

**Experimental demonstration of single-spin Stirling engine cycles with enhanced efficiency**P.-D. Li <sup>1,2,\*</sup> G.-Y. Ding<sup>1,2,\*</sup> J.-Q. Zhang <sup>1,†</sup> Q. Yuan <sup>1,2</sup> S.-Q. Dai <sup>1,2</sup> T.-H. Cui<sup>1,2</sup> F. Zhou,<sup>1,3</sup> L. Chen <sup>1,3,‡</sup>  
Q. Zhong,<sup>4</sup> H. Jing,<sup>5,§</sup> Ş. K. Özdemir,<sup>4,||</sup> and M. Feng <sup>1,3,6,¶</sup><sup>1</sup>State Key Laboratory of Magnetic Resonance and Atomic and Molecular Physics, *Wuhan Institute of Physics and Mathematics, Innovation Academy of Precision Measurement Science and Technology, Chinese Academy of Sciences, Wuhan 430071, China*<sup>2</sup>School of Physics, *University of the Chinese Academy of Sciences, Beijing 100049, China*<sup>3</sup>Research Center for Quantum Precision Measurement, *Guangzhou Institute of Industry Co. Ltd, Guangzhou 511458, China*<sup>4</sup>Department of Engineering Science and Mechanics, and Materials Research Institute, *Pennsylvania State University, University Park, State College, Pennsylvania 16802, USA*<sup>5</sup>Key Laboratory of Low-Dimensional Quantum Structures and Quantum Control of Ministry of Education, Department of Physics and Synergetic Innovation Center for Quantum Effects and Applications, *Hunan Normal University, Changsha 410081, China*<sup>6</sup>Department of Physics, *Zhejiang Normal University, Jinhua 321004, China*

(Received 4 February 2024; revised 2 January 2025; accepted 7 January 2025; published 21 January 2025)

Quantum heat engines (QHEs) employing Otto, Carnot, and Szilard cycles have already been demonstrated. Experimental demonstration of the quantum Stirling engine has been hindered due to the challenges in realizing a quantum isothermal process with qubits. Here, we experimentally execute a single-ion Stirling QHE and demonstrate that its efficiency is enhanced when dephasing is involved during the heat release strokes, which is contrary to the conventional viewpoint that dephasing deteriorates quantum features, resulting in reduced performance in QHEs. We also observe periodic oscillations in the heat absorption and the efficiency of the Stirling QHE, indicating the involvement of quantum coherence in the engine cycles. Our experiment is the first execution of Stirling QHE in a spin system, which may help better understand quantum thermodynamics and open new possibilities toward harnessing decoherence as a resource to improve the performance of QHEs.

DOI: [10.1103/PhysRevA.111.L010203](https://doi.org/10.1103/PhysRevA.111.L010203)

It is widely believed that quantum heat engines (QHEs), benefiting from quantum features, such as coherence and entanglement, can surpass the output power and efficiency of their classical counterparts. Microscopic and nanoscopic heat engines have already been implemented in various systems, such as single trapped ions [1–4], diamond nitrogen-vacancy centers [5], and so on [6–9], demonstrating the unique roles of quantum features in thermodynamics. Many routes to realize QHEs in superconducting circuits [10] and optomechanics [11,12] have also been put forward. Nevertheless, the Stirling heat engines, with the potential to achieve the highest efficiency of any real heat engine, have only been studied theoretically for their quantum version [13,14] and have been experimentally studied only in classical systems, such as single colloidal particles [15–17] and gas molecules in an acoustic traveling wave [18]. Realization of Stirling engine cycles in quantum systems remains largely unexplored.

In an effort to understand non-Hermitian dynamics of quantum heat engines, we have recently showed that reduced coherence during the isochoric stroke of a quantum Otto

engine (i.e., achieved in the experiments by executing this stroke in the broken phase) helps enhance its efficiency [3]. This counterintuitive observation is attributed to the fact that the reduced quantum coherence suppresses the heat absorption during the isochoric cooling stroke, thereby enhancing the engine efficiency without affecting the work done.

In this Letter, we report the experimental execution of single-spin Stirling QHE cycles in a trapped-ion system, in which we also elucidate the role of dephasing during the heat release cycles of the QHE on its efficiency and output power. We show that, contrary to conventional expectations, the efficiency of the cycle is improved when dephasing is elaborately introduced. Different from the observations in Ref. [3], in the present work related to Stirling engine, the oscillations observed in engine efficiency and heat absorption are originated from the accumulated dynamic phase [19–25], which implies the presence of quantum coherence in the characteristic quantities of the QHE. Dephasing introduced in the heat release strokes helps lower the oscillations, i.e., reducing the unexpected heat absorption and thus enhancing efficiency of the quantum heat engine. Monitoring the changes in the oscillations of thermodynamic quantities helps elucidate the relationship between the coherence and performance of QHEs.

Our experiment is carried out by employing the internal states of a single ultracold  $^{40}\text{Ca}^+$  ion confined in a surface-electrode trap (SET), as shown in Fig. 1(a). This SET is a 500- $\mu\text{m}$ -scale planar trap, similar to those employed

\*These authors contributed equally to this work.

†Contact author: changjianqi@gmail.com

‡Contact author: liangchen@wipm.ac.cn

§Contact author: jinghui73@foxmail.com

||Contact author: sko9@psu.edu

¶Contact author: mangfeng@wipm.ac.cn

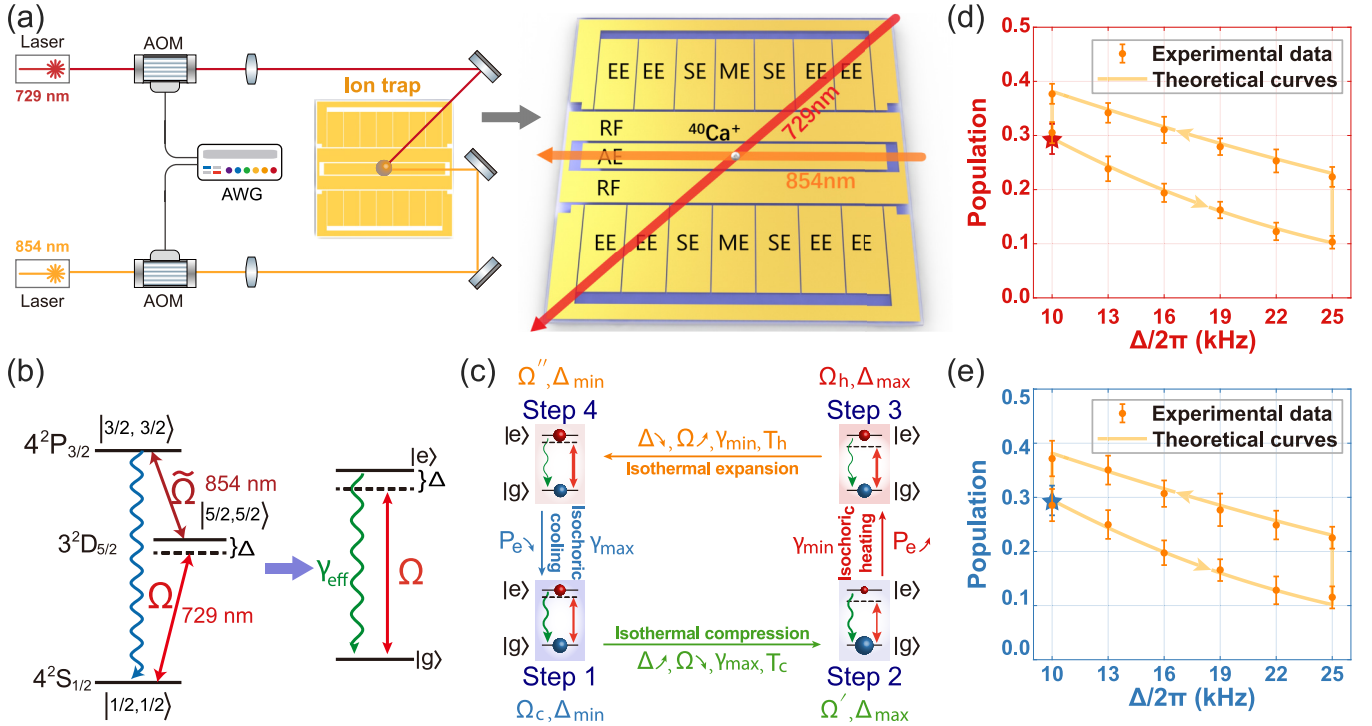


FIG. 1. (a) Schematic of the experimental setup. AOM: acousto-optic modulator. AWG: arbitrary waveform generator. A single ultracold  $^{40}\text{Ca}^+$  ion, confined in a SET, performs as the working substance of the Stirling QHE. The top view of the SET demonstrates seven pairs of side electrodes, two radio-frequency electrodes (RF), and an axial electrode (AE). The symbols on the electrodes are for convenience of discussion, where EE, SE, and ME represent, respectively, the end electrode, side-control electrode, and middle electrode. (b) Energy-level diagram of the ion, where the straight red arrows denote the transitions with Rabi frequencies  $\Omega$  and  $\tilde{\Omega}$  driven by 729-nm and 854-nm lasers, respectively, and  $\Delta$  is the detuning between the energy level and 729-nm laser. The blue wavy arrow represents the spontaneous emission with decay rate  $\Gamma$ . Such a three-level configuration reduces to an effective two-level system with tunable driving and decay. (c) Four strokes of the quantum Stirling cycle where strokes from step 1 to step 2 and from step 3 to step 4 represent isothermal processes, while strokes from step 2 to step 3 and from step 4 to step 1 are isochoric processes. (d) and (e) Detuning-population ( $\Delta$ - $P_e$ ) diagrams for the Stirling QHE without dephasing (d) and with dephasing (e), in which the experimental starting points are the red star (d) and blue star (e). The dephasing involved is mainly reflected in the larger error bars.

previously in Refs. [26–28] while more complicated, where the secular frequencies are  $\omega_z/2\pi = 0.65$  MHz,  $\omega_x/2\pi = 1.2$  MHz, and  $\omega_y/2\pi = 1.59$  MHz, respectively. The confined ion stays stably above the surface of the SET by  $500\ \mu\text{m}$ . Under an external magnetic field of  $0.512$  mT directed along axial orientation, the ground state  $4^2S_{1/2}$  and the metastable state  $3^2D_{5/2}$  are split into two and six Zeeman energy sub-levels, respectively. As plotted in Fig. 1(b), we label the ground state  $|4^2S_{1/2}, m_J = +1/2\rangle$  as  $|g\rangle$ , the metastable state  $|3^2D_{5/2}, m_J = +5/2\rangle$  as  $|e\rangle$  and  $|4^2P_{3/2}, m_J = +3/2\rangle$  as  $|p\rangle$ . We perform Doppler and resolved sideband cooling of the ion to reduce the average phonon number of the  $z$  axis motional mode. With the 729-nm or 854-nm lasers ON [see Fig. 1(b)], the three-level system reduces to an effective two-level system representing a qubit [30], which is used in this work as the working substance of the Stirling QHE.

The dynamical evolution of the effective two-level model is governed by the Lindblad master equation,  $\dot{\rho} = \mathcal{L}\rho = -i[H, \rho] + \frac{\gamma_{\text{eff}}}{2}(2\sigma_- \rho \sigma_+ - \sigma_+ \sigma_- \rho - \rho \sigma_+ \sigma_-) + \frac{\gamma_p}{2}(2\sigma_z \rho \sigma_z - \rho \sigma_z \sigma_z - \sigma_z \sigma_z \rho)$ , where  $\mathcal{L}$  is the Liouvillian superoperator,  $\rho$  denotes the density operator, and  $\gamma_{\text{eff}}$  and  $\gamma_p$  represent the effective decay rate from  $|e\rangle$  to  $|g\rangle$  and the dephasing rate, respectively. Here, the total Hamiltonian is

$H = \Delta|e\rangle\langle e| + \frac{\Omega}{2}(|e\rangle\langle g| + |g\rangle\langle e|)$ , where  $\Delta$  represents the frequency detuning between the resonance transition and the driving laser while  $\Omega$  denotes the Rabi frequency.

In our experiment, the Stirling cycles are executed by tuning  $\Omega$  and  $\gamma_{\text{eff}}$  using the semiconductor lasers. We monitor the variation of the population of  $|e\rangle$ , from which we obtain the required thermodynamic quantities such as work, heat, and efficiency. The temperature  $T$  of a spin system is defined as  $T = \Delta/[k_B \ln(P_e/P_g)]$  [31], where  $P_e$  and  $P_g$  denote, respectively, the populations of the states  $|e\rangle$  and  $|g\rangle$ ;  $\Delta = E_e - E_g - \hbar\omega_l$  is the effective energy gap between  $|e\rangle$  and  $|g\rangle$  in the interaction representation where  $\omega_l$  represents the 729-nm laser frequency; and  $k_B$  is the Boltzmann constant.

A typical Stirling heat engine cycle has four strokes: two isothermal strokes and two isochoric strokes. Quantum Stirling cycles are different from their classical counterparts in the definition of thermodynamic quantities. In a quantum isochoric stroke, the population  $P_n$  of each level of the qubit changes until the working substance reaches thermal equilibrium with the heat bath, while the detuning  $\Delta$  stay constant. In the quantum isothermal strokes, on the other hand, the populations in  $|e\rangle$  and  $|g\rangle$  change along with the energy gap  $\Delta$  so as to keep the effective temperature  $T$  unchanged [32].

In our system, we execute the ingredients of the Stirling QHE cycles as follows: We prepare the hot and cold heat baths by tuning the ratio of the effective decay rate  $\gamma_{\text{eff}}$  to the Rabi frequency  $\Omega$ . This indicates that laser irradiation and the real environment constitute the baths together, where the strong laser drive corresponds to the hot bath, and the weak laser drive plus the real environment is considered as the cold bath. The qubit completes heat absorption and heat release strokes through its coupling to hot and cold baths, respectively. By monitoring the variation of  $P_e$ , we calculate the work produced in the system and the heat absorbed from the hot bath, which allows us to quantify the performance of the whole Stirling cycle.

In the rotating frame with respect to the driving laser frequency, quantum isothermal strokes are implemented by tuning the frequency of the 729-nm driving laser together with  $\gamma_{\text{eff}}/\Omega$ , which helps to keep the temperature of the working substance invariant. Similarly, quantum isochoric strokes are implemented by tuning  $\gamma_{\text{eff}}/\Omega$ , which manipulates the heat exchange between the working medium and the thermal baths. Thus, while the qubit decay is tuned by adjusting the power of the 854-nm laser, the frequency and the power of the 729-nm laser helps implement the four strokes of the Stirling cycle as follows [Fig. 1(c)]. By setting  $\Delta = \Delta_{\text{min}}$ ,  $\gamma_{\text{eff}} = \gamma_{\text{max}}$ , and  $\Omega = \Omega_c$ , we prepare the qubit initially at a steady state with  $P_e = 0.3$  (step 1). Starting from this initial state, we first carry out an isothermal compression stroke by increasing the detuning  $\Delta$  linearly from  $\Delta_{\text{min}}$  to  $\Delta_{\text{max}}$ , where  $\gamma_{\text{eff}}$  is kept at its maximum value  $\gamma_{\text{max}}$  (step 1  $\rightarrow$  step 2). During this process, the drive strength is decreased from  $\Omega_c$  to  $\Omega'$  to keep the effective temperature  $T_c = 0.56 \mu\text{K}$ , where  $T_c$  represents the temperature of the cold bath. Next, we perform the isochoric heating by rapidly increasing  $\Omega$  to a large value  $\Omega_h$  and decreasing  $\gamma_{\text{eff}}$  to  $\gamma_{\text{min}}$ , during which  $\Delta$  remains equal to  $\Delta_{\text{max}}$  (step 2  $\rightarrow$  step 3). Then, we execute an isothermal expansion by linearly decreasing  $\Delta$  from  $\Delta_{\text{max}}$  to  $\Delta_{\text{min}}$  with  $\gamma_{\text{eff}} = \gamma_{\text{min}}$  staying unchanged (step 3  $\rightarrow$  step 4), during which  $\Omega$  is increased from  $\Omega_h$  to  $\Omega''$  to keep  $T_h = 0.98 \mu\text{K}$ . Here,  $T_h$  denotes the temperature of the hot bath. Finally, we perform the isochoric cooling by rapidly decreasing  $\Omega$  to  $\Omega_c$  and meanwhile increasing  $\gamma_{\text{eff}}$  to  $\gamma_{\text{max}}$  (step 4  $\rightarrow$  step 1). To accomplish a closed Stirling cycle, we wait for the system to reach a steady state, returning to the initial state after finishing the last stroke. To further clarify the process, we provide detuning-population ( $\Delta$ - $P_e$ ) diagrams of our experimental implementation of Stirling QHE in Figs. 1(d) and 1(e) [33].

We first consider the scenario without dephasing. We observe in Fig. 2(a) that the population  $P_e$  exhibits a hump in the second stroke (i.e., the isochoric heating) and a ramp in the fourth stroke (i.e., the isochoric cooling), which reflect the presence of quantum coherence and agree with the results obtained from the simulation of the master equation. The population oscillations are also seen during the first and third strokes (isothermal compression and expansion strokes) due to the variation of  $\Delta$  and  $\Omega$ . We also note in Fig. 2(b) that the temperature is not constant as expected theoretically, but oscillating in the first and third strokes. This deviation can be attributed to the experimental imperfection, i.e., discretely tuning the 729-nm laser frequency in sequence, rather than in a continuous fashion.

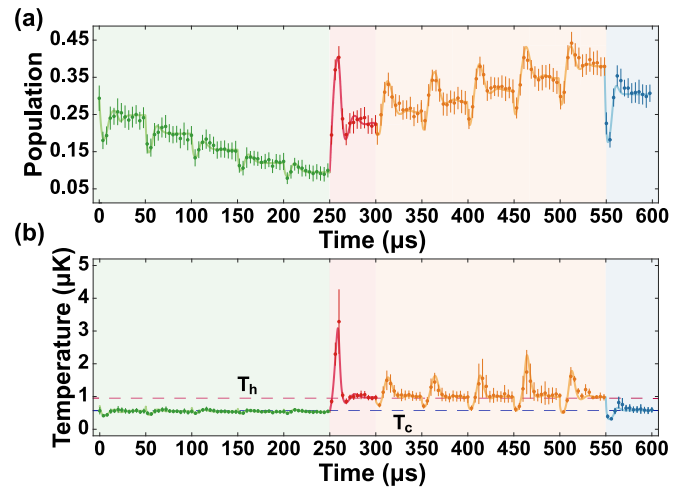


FIG. 2. Stirling QHE cycle without dephasing. (a) Time evolution of measured population of the excited state, where the periodicity of 50  $\mu\text{s}$  originates from five sequential changes of  $\Delta$  with steps of 50  $\mu\text{s}$ . (b) Variation of the effective temperature of the system in time. The solid curves are obtained by simulating master equations. The circles and error bars represent, respectively, the average and standard deviations of 10 000 measurements. Dashed blue and red lines represent the temperatures of the cold and hot baths, respectively. Regions with different colors represent different strokes of the Stirling cycle, with the green, pink, orange, and blue corresponding to the first (isothermal compression), second (isochoric heating), third (isothermal expansion), and fourth (isochoric cooling) strokes, respectively. The first (green) and the third (orange) strokes are executed by up- and down-scanning the detuning  $\Delta$  between  $\Delta_{\text{min}}/2\pi = 10 \text{ kHz}$  and  $\Delta_{\text{max}}/2\pi = 25 \text{ kHz}$ , respectively, with constant  $\gamma_{\text{eff}}$ . Rabi frequencies are varied from  $\Omega_c/2\pi = 45.8 \text{ kHz}$  to  $\Omega'/2\pi = 24.9 \text{ kHz}$  and  $\Omega_h/2\pi = 40.2 \text{ kHz}$  to  $\Omega''/2\pi = 53.6 \text{ kHz}$  in the first and third strokes, respectively. The second (pink) and the fourth (blue) strokes are implemented by increasing and decreasing  $\Omega/\gamma_{\text{eff}}$  with constant detuning rapidly. The decay rates we used are  $\gamma_{\text{max}} = 280 \text{ kHz}$  in the first and fourth strokes and  $\gamma_{\text{min}} = 180 \text{ kHz}$  in the second and third strokes. The durations of the four strokes are, respectively,  $T_1 = T_3 = 250 \mu\text{s}$ ,  $T_2 = T_4 = 50 \mu\text{s}$ .

Next, we consider the case where the Stirling cycle is exposed to dephasing. For this purpose, we generate white noise signal using an arbitrary waveform generator (AWG) and apply this noise signal to the acousto-optic modulator (AOM), which modulates the light from the 729-nm laser [Fig. 1(a)]. This subsequently introduces phase noise to the light field that helps control the internal state of the trapped ion, thereby introducing an effective dephasing to the qubit. As discussed above, the AOM modulated light from the 729-nm laser is used to implement the strokes of a Stirling engine cycle. Since the population variation would change the heat absorption, we expect to reduce the heat absorption by suppressing the population via the dephasing introduced in isochoric cooling and isothermal compression strokes, and thus enhance the efficiency of the Stirling QHE. Here, we consider the dephasing rate to be  $\gamma_p = 500 \text{ kHz}$ , and keep  $T_h$  and  $T_c$  the same as those used in the absence of dephasing. We observe in Fig. 3(a) that the ramps and humps of  $P_e$  in the first and fourth strokes are shrunken compared to Fig. 2(a) due to quantum

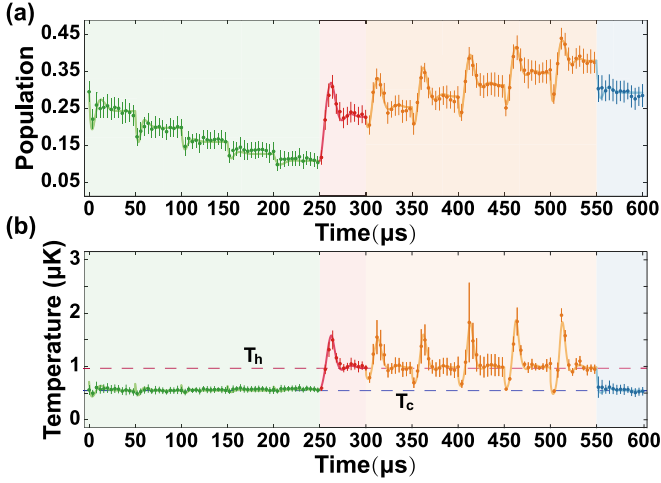


FIG. 3. Stirling QHE cycle with dephasing introduced in the first and fourth strokes. (a) Time evolution of measured population of the excited state. (b) Variation of the effective temperature of the system in time. The solid curves are obtained by simulating master equations. The circles and error bars represent, respectively, the average and standard deviations of 10 000 measurements. Dashed blue and red lines represent the temperatures of cold and hot baths, respectively. Regions with different colors represent different strokes of the whole cycle, with the green, pink, orange, and blue corresponding to the first (isothermal compression), second (isochoric heating), third (isothermal expansion), and fourth (isochoric cooling) strokes, respectively. The first (green) and the third (orange) strokes are executed by up- and down-scanning the detuning  $\Delta$  between  $\Delta_{\min}/2\pi = 10$  kHz and  $\Delta_{\max}/2\pi = 25$  kHz, respectively, with constant  $\gamma_{\text{eff}}$ . Rabi frequencies are varied from  $\Omega_c/2\pi = 70.7$  kHz to  $\Omega'_c/2\pi = 29.9$  kHz and  $\Omega_h/2\pi = 40.2$  kHz to  $\Omega''_h/2\pi = 53.6$  kHz in the first and third strokes, respectively. The second (pink) and the fourth (blue) strokes are implemented by increasing and decreasing  $\Omega/\gamma_{\text{eff}}$  with constant detuning rapidly. The decay rates we used are  $\gamma_{\text{max}} = 280$  kHz in the first and fourth strokes and  $\gamma_{\text{min}} = 180$  kHz in the second and third strokes. The dephasing rate is set to be  $\gamma_p = 500$  kHz. The durations of the four strokes are, respectively,  $T_1 = T_3 = 250 \mu\text{s}$  and  $T_2 = T_4 = 50 \mu\text{s}$ . The  $50 \mu\text{s}$  periodicity seen in the plots originates from five sequential changes of  $\Delta$  with steps of  $50 \mu\text{s}$ .

coherence reduced largely by the dephasing effect. Similarly, the effective temperature in the second stroke of Fig. 3(b) is smaller than that in Fig. 2(b).

Since the system returns to its initial state after completion of the cycle, we can evaluate the net work using  $W_{\text{net}} = \text{Tr}[-\int_0^t \rho(t) dH(t)]$ , where  $\rho(t)$  represents the state of the two-level system governed by  $H(t) = \Delta(t)|e\rangle\langle e|$ . The corresponding heat in the engine cycles is given by  $Q_{\text{in(out)}} = \text{Tr}[\int_0^t H(t) d\rho(t)]$  for  $\delta P_e > 0$  ( $\delta P_e < 0$ ). Since no work is produced during isochoric strokes, here we only consider the first and the third strokes, which respectively execute isothermal compression and expansion. We note that during the isothermal compression process the bath performs work on the system while in the isothermal expansion process the system performs work.

We evaluate the role of quantum coherence in the performance of the Stirling QHE cycle by monitoring the

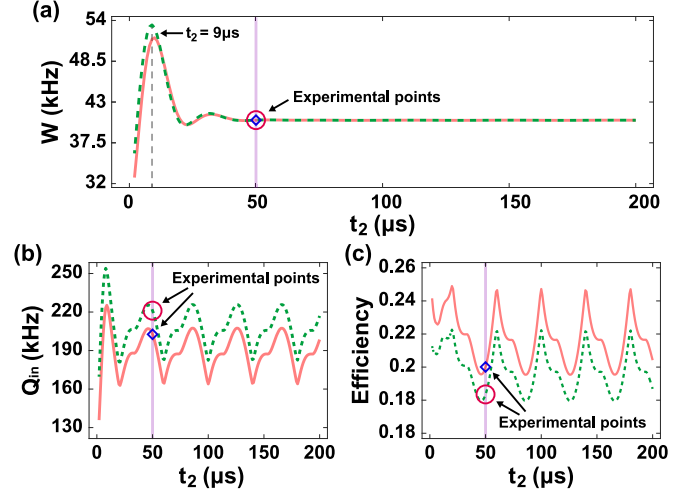


FIG. 4. Stirling QHE cycle with or without dephasing introduced in the first and fourth strokes. (a) The net work. (b) The heat absorption in the whole cycle. (c) The efficiency as a function of the second stroke execution time  $t_2$ , while execution times of all other strokes are kept fixed. The pink solid lines and green dashed lines represent Stirling QHE cycles with or without dephasing, respectively. The red circle and the blue diamond together with the vertical solid line denote the operating condition of the cycles implemented in the experiments. The dephasing rate is set to be  $\gamma_p = 500$  kHz.

oscillations in  $P_e$  in the isochoric and isothermal strokes, and then calculate the net work, heat absorption, and efficiency of the Stirling QHE cycle as a function of the execution time of the second stroke (i.e., the isochoric heating) while keeping the execution time of other strokes fixed [Fig. 4(a)]. We observe a clear hump at  $t_2 = 9 \mu\text{s}$  as an indication of the role of quantum coherence in the second stroke on the net work. When  $t_2$  is long enough such that the system reaches its steady state in the second stroke, the net work without dephasing in the cycle is the same as that with dephasing. This is due to the fact that, under the same  $T_c$  and  $T_h$  and the same detuning ranges, the work production is only relevant to the population of the reached steady state when we vary  $\Delta$  and  $\Omega$  in the isothermal strokes.

Heat absorption during the isothermal compression and isochoric cooling strokes occurs only in quantum systems due to the quantum coherence involved [i.e., see the ramps in Figs. 2(a) and 3(a)]. By tuning the execution time of the second stroke, we observe the periodic oscillation of heat absorption  $Q_{\text{in}}$  in the whole cycle when the system reaches its steady state, which originates from the accumulated dynamic phase [33]. Here, the oscillation period is  $\tau = 2\pi/\Delta_{\max} = 40 \mu\text{s}$ .

We observe in Fig. 4 that the net work is irrelevant to the introduced dephasing, while the heat absorption decreases with dephasing, leading to an enhanced efficiency in the QHE cycle. This can be understood as follows: First, the net work in a Stirling QHE strongly depends on the heat bath temperatures ( $T_c$  and  $T_h$ ) and the detuning ranges. Since we have the values of these parameters fixed, the net work is also fixed. Second, the efficiency of the engine decreases due to heat absorption during the isochoric cooling stroke. This is a result of the

presence of quantum coherence. The dephasing intentionally introduced in the system reduces the coherence, thereby suppressing heat absorption during the cooling stroke, which in turn enhances the engine efficiency.

Additionally, we have also observed the periodic oscillations of both the heat absorption and the efficiency, reflecting that, despite dephasing involved, quantum coherence still remains and contributes to the thermodynamic cycle. We note that in a previous work [3] involving Otto QHE cycles, we did not observe any oscillation in efficiency and heat absorption. This results from the adiabatic expansion process, in which the quantum state is invariant. Although phases are accumulated in the isochoric heating process, oscillations induced by these phases are completely suppressed in the subsequent adiabatic process. In contrast, in the Stirling QHE cycle, the isochoric stroke is followed by the isothermal stroke, in the latter of which the accumulated phases lead to oscillatory behavior in the efficiency and absorbed heat. As a result, the Stirling QHE is more suitable for exhibiting quantum characteristics in the heat and efficiency.

In conclusion, we have experimentally executed the Stirling QHE cycle in a single trapped-ion system. By introducing dephasing, we have acquired enhanced efficiency due to the reduced heat absorption. This indicates that coherence is essential to the performance of QHEs, which however must

be elaborately used. The observed oscillation is also the difference of the Stirling QHE from the Otto counterpart, reflecting that the quantum nature of isothermal processes are different from that of adiabatic processes. Our experiments help develop a deeper understanding of the behavior of Stirling heat engines in quantum mechanical settings and may open up new avenues in harnessing decoherence as a resource to improve the performance of quantum systems. Future work would focus on the work output from the engine to quantum loads, which would be more practical in application of quantum engines, but need more careful effort on defining work and heat in the quantum regime [34,35].

We thank Franco Nori for critically reading this manuscript. This work was supported by the National Natural Science Foundation of China under Grants No. U21A20434, No. 12074390, No. 12304315, and No. 12074346; by Key Lab of Guangzhou for quantum precision measurement under Grant No. 202201000010; by Guangdong Provincial Quantum Science Strategic Initiative under Grant No. GDZX2305004; and by Nansha Senior Leading Talent Team Project under Grant No. 2021CXTD02. S.K.O. acknowledges the support from Air Force Office of Scientific Research (AFOSR) Multidisciplinary University Research Initiative (MURI) Award No. FA9550-21-1-0202.

- 
- [1] J. Roßnagel, S. T. Dawkins, K. N. Tolazzi, O. Abah, E. Lutz, F. Schmidt-Kaler, and K. Singer, A single-atom heat engine, *Science* **352**, 325 (2016).
  - [2] D. von Lindenfels, O. Gräß, C. T. Schmiegelow, V. Kaushal, J. Schulz, M. T. Mitchison, J. Goold, F. Schmidt-Kaler, and U. G. Poschinger, Spin heat engine coupled to a harmonic-oscillator flywheel, *Phys. Rev. Lett.* **123**, 080602 (2019).
  - [3] J.-W. Zhang, J.-Q. Zhang, G.-Y. Ding, J.-C. Li, J.-T. Bu, B. Wang, L.-L. Yan, S.-L. Su, L. Chen, F. Nori, Ş. K. Özdemir, F. Zhou, H. Jing, and M. Feng, Dynamical control of quantum heat engines using exceptional points, *Nat. Commun.* **13**, 6225 (2022).
  - [4] J.-T. Bu, J.-Q. Zhang, G.-Y. Ding, J.-C. Li, J.-W. Zhang, B. Wang, W.-Q. Ding, W.-F. Yuan, L. Chen, Ş. K. Özdemir, F. Zhou, H. Jing, and M. Feng, Enhancement of quantum heat engine by encircling a Liouvillian exceptional point, *Phys. Rev. Lett.* **130**, 110402 (2023).
  - [5] J. Klatzow, J. N. Becker, P. M. Ledingham, C. Weinzettl, K. T. Kaczmarek, D. J. Saunders, J. Nunn, I. A. Walmsley, R. Uzdin, and E. Poem, Experimental demonstration of quantum effects in the operation of microscopic heat engines, *Phys. Rev. Lett.* **122**, 110601 (2019).
  - [6] C. A. Ryan, O. Moussa, J. Baugh, and R. Laflamme, Spin based heat engine: Demonstration of multiple rounds of algorithmic cooling, *Phys. Rev. Lett.* **100**, 140501 (2008).
  - [7] J. P. S. Peterson, T. B. Batalhão, M. Herrera, A. M. Souza, R. S. Sarthour, I. S. Oliveira, and R. M. Serra, Experimental characterization of a spin quantum heat engine, *Phys. Rev. Lett.* **123**, 240601 (2019).
  - [8] J. V. Koski, V. F. Maisi, J. P. Pekola, and D. V. Averin, Experimental realization of a Szilard engine with a single electron, *Proc. Natl. Acad. Sci. USA* **111**, 13786 (2014).
  - [9] K. Ono, S. N. Shevchenko, T. Mori, S. Moriyama, and F. Nori, Analog of a quantum heat engine using a single-spin qubit, *Phys. Rev. Lett.* **125**, 166802 (2020).
  - [10] H. T. Quan, Y. D. Wang, Y. X. Liu, C. P. Sun, and F. Nori, Maxwell demon assisted thermodynamic cycle in superconducting quantum circuits, *Phys. Rev. Lett.* **97**, 180402 (2006).
  - [11] K. Zhang, F. Bariani, and P. Meystre, Quantum optomechanical heat engine, *Phys. Rev. Lett.* **112**, 150602 (2014).
  - [12] A. Dechant, N. Kiesel, and E. Lutz, All-optical nanomechanical heat engine, *Phys. Rev. Lett.* **114**, 183602 (2015).
  - [13] S. Hamedani Raja, S. Maniscalco, G. S. Paraoanu, J. P. Pekola, and N. Lo Gullo, Finite-time quantum Stirling heat engine, *New J. Phys.* **10**, 045005 (2008).
  - [14] X.-L. Huang, X.-Y. Niu, X.-M. Xiu, and X.-Y. Yi, Quantum Stirling heat engine and refrigerator with single and coupled spin systems, *Eur. Phys. J. D* **68**, 32 (2014).
  - [15] V. Blickle and C. Bechinger, Realization of a micrometre-sized stochastic heat engine, *Nat. Phys.* **8**, 143 (2012).
  - [16] S. Krishnamurthy, S. Ghosh, D. Chatterji, R. Ganapathy, and A. K. Sood, A micrometre-sized heat engine operating between bacterial reservoirs, *Nature (London)* **12**, 1134 (2016).
  - [17] N. Roy, N. Leroux, A. K. Sood, and R. Ganapathy, Tuning the performance of a micrometer-sized Stirling engine through reservoir engineering, *Nat. Commun.* **12**, 4927 (2021).
  - [18] S. Backhaus and G. A. Swift, A thermoacoustic Stirling heat engine, *Nature (London)* **399**, 335 (1999).
  - [19] J. Anandan, The geometric phase, *Nature (London)* **360**, 307 (1992).
  - [20] R. Y. Chiao and Y.-S. Wu, Manifestations of Berry's topological phase for the photon, *Phys. Rev. Lett.* **57**, 933 (1986).
  - [21] A. Tomita and R. Y. Chiao, Observation of Berry's topological phase by use of an optical fiber, *Phys. Rev. Lett.* **57**, 937 (1986).

- [22] R. Y. Chiao, A. Antaramian, K. M. Ganga, H. Jiao, S. R. Wilkinson, and H. Nathel, Observation of a topological phase by means of a nonplanar Mach-Zehnder interferometer, *Phys. Rev. Lett.* **60**, 1214 (1988).
- [23] Y. B. Zhang, Y. W. Tan, H. L. Stormer, and P. Kim, Experimental observation of the quantum Hall effect and Berry's phase in graphene, *Nature (London)* **438**, 201 (2005).
- [24] C. G. Yale, F. J. Heremans, B. B. Zhou, A. Auer, G. Burkard, and D. D. Awschalom, Optical manipulation of the Berry phase in a solid-state spin qubit, *Nat. Photon.* **10**, 184 (2016).
- [25] J. Wang, S. Valligatla, Y. Yin, L. Schwarz, M. Medina-Sánchez, S. Baunack, C. H. Lee, R. Thomale, S. Li, V. M. Fomin, L. Ma, and O. G. Schmidt, Experimental observation of Berry phases in optical Möbius-strip microcavities, *Nat. Photon.* **17**, 120 (2023).
- [26] W. Wan, H. Y. Wu, L. Chen, F. Zhou, S. J. Gong, and M. Feng, Demonstration of motion transduction in a single-ion nonlinear mechanical oscillator, *Phys. Rev. A* **89**, 063401 (2014).
- [27] J. Li, L. L. Yan, L. Chen, Z. C. Liu, F. Zhou, J. Q. Zhang, W. L. Yang, and M. Feng, Ion-crystal demonstration of a temperature-driven structural phase transition, *Phys. Rev. A* **99**, 063402 (2019).
- [28] Z.-C. Liu, L. Chen, J. Li, H. Zhang, C. Li, F. Zhou, S.-L. Su, L.-L. Yan, and M. Feng, Structural phase transition of the ion crystals embedded in an optical lattice, *Phys. Rev. A* **102**, 033116 (2020).
- [29] J. W. Zhang, K. Rehan, M. Li, J. C. Li, L. Chen, S. L. Su, L. L. Yan, F. Zhou, and M. Feng, Single-atom verification of the information-theoretical bound of irreversibility at the quantum level, *Phys. Rev. Res.* **2**, 033082 (2020).
- [30] In our system, the transition  $|g\rangle \rightarrow |e\rangle$  is induced by a semiconductor laser (729 nm) tuned to the resonance transition. The dipolar transition  $|e\rangle$  to  $|p\rangle$  is achieved by a semiconductor laser (854 nm) under the restriction of the selection rule. Finally, the transition  $|p\rangle \rightarrow |g\rangle$  takes place as a spontaneous emission process which is also restricted by the selection rules. In this model, we can engineer both the Rabi frequency  $\Omega$  and the effective decay rate  $\gamma_{\text{eff}} = \tilde{\Omega}^2/\Gamma$  under the condition of  $\Omega \ll \tilde{\Omega}$  [3,29]. With this level of controllability, we can tune this two-level system to perform Stirling QHE cycles.
- [31] H. T. Quan, Y.-X. Liu, C. P. Sun, and F. Nori, Quantum thermodynamic cycles and quantum heat engines, *Phys. Rev. E* **76**, 031105 (2007).
- [32] Execution of the isothermal strokes requires to elaborately control the frequency and strength of the 729-nm laser (relevant to the detuning and Rabi frequency, respectively), which remains the temperature  $T$  to be constant during the strokes. Meanwhile, the isothermal strokes are required to be accomplished at steady states. As shown later, in our experimental execution of the quantum Stirling heat engine, we have tried to reach nearly equilibrium states after long time evolution, in which we implement the variation of detuning by five pulse sequences with equal steps of 50 ms. The technical challenge lies in keeping some coherence in the system after accomplishing the isothermal strokes, which is essential to a quantum heat engine.
- [33] See Supplemental Material at <http://link.aps.org/supplemental/10.1103/PhysRevA.111.L010203> for more details of thermodynamic processes and quantities of interest.
- [34] The potential quantum load could be one of the vibrational degrees of freedom of the ion or an additional ion. For the former, we may consider connecting the spin to the vibrational mode by a Jaynes-Cummings interaction. For the latter, we may couple the two ions by spin entanglement operations. In the execution of the quantum Stirling engine, we need to decouple the engine from the quantum load in the isothermal expansion and compression strokes. After accomplishing the engine cycle, we make appropriate measurement on the quantum load, which would help evaluate the output work from the quantum Stirling engine. However, the coupling of the engine's working medium and the quantum load develops correlations between them and thus would increase information entropy in the load. So, we should be more careful to define the work measured in this case. An alternative is to just consider energy conversion, instead of work or heat output, from a quantum engine to a quantum load [35].
- [35] J.-W. Zhang, B. Wang, W.-F. Yuan, J.-C. Li, J.-T. Bu, G.-Y. Ding, W.-Q. Ding, L. Chen, F. Zhou, and M. Feng, Energy-conversion device using a quantum engine with the work medium of two-atom entanglement, *Phys. Rev. Lett.* **132**, 180401 (2024).